Geophysical Journal International

Geophys. J. Int. (2015) **203,** 428–436
GJI Seismology

doi: 10.1093/gji/ggv290

Controls on radon emission from granite as evidenced by compression testing to failure

Katsuaki Koike,[1] Tohru Yoshinaga,[2] Kenta Suetsugu,[3] Koki Kashiwaya[1] and Hisafumi Asaue[4,*]

[1]*Laboratory of Environmental Geosphere Engineering, Graduate School of Engineering, Kyoto University, Katsura, Kyoto, Japan. E-mail: koike.katsuaki.5x@kyoto-u.ac.jp*
[2]*Technical Division, Faculty of Engineering, Kumamoto University, Kumamoto, Japan*
[3]*Koken Boring Machine Co., Ltd., Tokyo, Japan*
[4]*Graduate School of Science and Technology, Kumamoto University, Kumamoto, Japan*

Accepted 2015 July 7. Received 2015 July 7; in original form 2015 April 2

SUMMARY

A set of uniaxial compression tests of granite specimens taken from five localities across Japan was conducted to identify the factors controlling the quantity of radon (Rn) emission (sum of ^{222}Rn and ^{220}Rn) during compression and failure. An α-scintillation detector and a gas flow unit were installed with a testing machine to enable continuous measurement of Rn emissions. Common to all specimens, Rn emissions remained at or slightly declined from the background level after the start of loading; this is similar to the natural phenomenon of decline in groundwater-dissolved Rn before an earthquake. Closure of original microcracks is the most likely cause of the initial Rn decline. Then, Rn emissions begin to increase at 46–57 per cent stress level to the uniaxial compressive strength, and continue to increase even after the failure of specimen. This commencement stress level is close to the general stress level at outbreak of acoustic emissions caused by the development and connection of microcracks. The Rn increase after failure is similar to a phenomenon observed in aftershocks, which may originate from the enhancement of Rn emanations from grains due to the large increase in total surface area and stress release. In addition to the initial radioelement content in rock, the failure pattern (conjugate shear versus longitudinal tensile type), compressive strength, and grain size are possible control factors of the maximum quantity of Rn emissions induced by failure. This maximum may also be affected by the development velocity of the emanation area, which is related to the Rn emanation fraction, associated with the fragmentation. In addition to the magnitude of an earthquake and its hypocentre distance to Rn detectors, the magnitude of increase in Rn concentration in soil gas and groundwater before, during, and after an earthquake in crystalline rocks depends on the intrinsic radioelement content, the mineral texture, and the mechanical properties of rocks. Rock fracturing and failure do not necessarily induce increase in Rn emission due to these rock properties, which can be used to understand the sensitivity of Rn concentration in soil gas or groundwater in connection with an earthquake.

Key words: Fracture and flow; Earthquake interaction, forecasting, and prediction; Fractures and faults.

1 INTRODUCTION

Radon (Rn) has been the most commonly examined radioelement in investigations of fracture-related structures and geodynamics in the Earth's crust. Two abundant isotopes are used in Rn applications: ^{222}Rn generated in the uranium (^{238}U) series, and ^{220}Rn in the thorium (^{232}Th) series. The half-life of ^{222}Rn (3.58 d) is 6000 times longer than that of ^{220}Rn (53.4 s).

The pervasive use of Rn is due to its peculiar properties as an inert gas that migrates in the crust during its half-life and is detectable at low concentration. Representative applications include: change in Rn concentration in soil gas and dissolved in groundwater before, during, and after earthquakes (e.g. Wakita 1996; İnan *et al.* 2008; Cicerone *et al.* 2009; Jordan *et al.* 2011), fault localization from Rn concentration enhancement (e.g. Neri *et al.* 2011; Wang *et al.* 2014), delineation of fault geometry by a combination of spatial Rn

*Now at: Laboratory on Innovative Techniques for Infrastructures, Graduate School of Engineering, Kyoto University, Katsura, Kyoto, Japan.

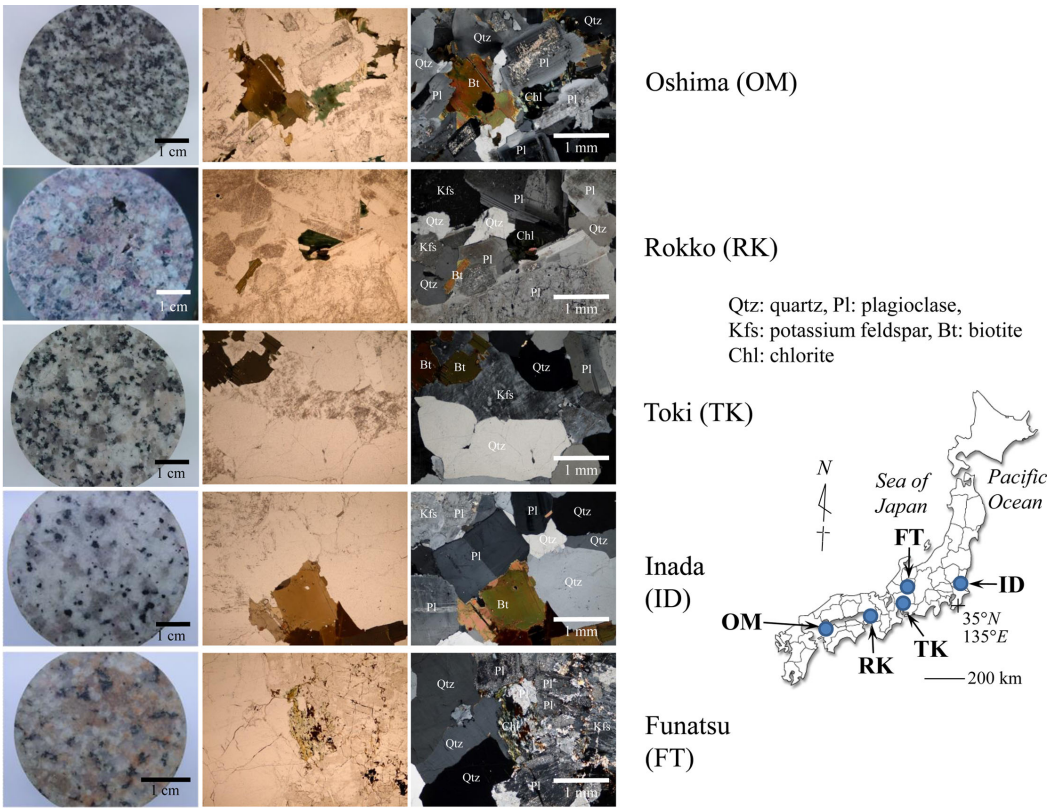

Figure 1. Sampling places and photos of granite specimens. Mineralogical features such as mineral composition, grain size and development of microcracks are shown in the parallel and crossed-Nicol photos of thin-sections.

concentration and numerical simulation of Rn transport (Koike *et al.* 2009), Rn concentration change induced by eruption (e.g. Connor *et al.* 1996; Neri *et al.* 2006; Cigolini *et al.* 2007), and use of Rn as a tracer of temperature and pressure changes in geothermal reservoir (Koike *et al.* 2014a). One recent finding is a strong correlation between Rn concentration in soil gas and the cumulated energy of nearby and recent earthquakes, ascribed to the increase in pore pressure around the Rn source at depth that is caused by frequently induced strain (Koike *et al.* 2014b). Rn changes associated with earthquakes have been observed in many areas since the 1950s (e.g. Scholz *et al.* 1973), and there is a controversial expectation, unproven, that Rn is a precursor indicator of earthquake.

Continuous measurement of Rn concentrations in soil gas and groundwater has been possible since the 1990s, and deployed detectors have characterized the Rn concentration changes associated with earthquakes for decades across Japan and elsewhere. From many global observations, coseismic enhancement of Rn concentration is seen to be a common phenomenon, while Rn concentrations before earthquakes have been variable, including measurements that are unchanged, increased or decreased. Characteristics of coseismic Rn enhancement also differ between occurrences, including timing, amount and spatial distribution of the increase.

To simulate at a laboratory scale the Rn concentration change induced by strain enhancement, microcracking and failure of intact rock, four types of geo-materials have been used as specimens for uniaxial or triaxial compression tests, including granite (Holub & Brady 1981; Katoh *et al.* 1984, 1985; Hishinuma *et al.* 1999; Nicolas *et al.* 2014) and low porosity lava (Mollo *et al.* 2011) as crystalline rock, lithophysae-rich tuff as porous media (Tuccimei *et al.* 2010) and concrete as a fault-zone materials model (King & Luo 1990). The following phenomena were observed common to these four geomaterials: Rn decline by closure of pores and pre-existing microcracks at low stress levels; large Rn enhancement by development of micro- and macrocracks; and continuation of Rn increase after failure, caused by increase in emanation area in the fragmented specimens. However, reasons for the variable pre-earthquake patterns and coseismic enhancement quantities have not been clarified by these experiments.

Granite is the most common rock type in the surface geology and basement of Japan. Because of its brittleness, many earthquakes with different magnitudes have occurred in granitic areas (e.g. Asaue *et al.* 2007; Iidaka *et al.* 2009), which means that Rn emissions in the upper crust of Japan are typically the product of releases from granite. Granite as a class has a variety of mineral compositions and grain sizes, mechanical properties such as strength and toughness, and content of radioelements. Although the Rn studies based on compression of specimens have accumulated, the effects of the mineralogical and mechanical properties of granite on the Rn emission quantity have not been sufficiently clarified. Consequently, this study was designed to use a set of granite specimens taken from different places in Japan to elucidate the effects and the control factors of variable granite properties on the Rn quantity released by uniaxial compression testing. The results contribute to explanation of variable Rn properties in connection with earthquake, and show the conditions for emergence of precursory Rn anomaly in soil gas and groundwater.

2 GRANITE SAMPLES

Five types of granite from areas across Japan were selected for the present experiments (Fig. 1): Oshima granite (OM) from Yamaguchi

prefecture in southwest Japan; Rokko granite (RK) from Hyogo prefecture in west Japan; Toki granite (TK) and Funatsu granite (FT) from Gifu prefecture in central Japan; and Inada granite (ID) in Ibaraki prefecture in east Japan. Geological ages of the granites are FT: Triassic to Jurassic; OM and TK: Late Cretaceous; RK: Latest Cretaceous; and ID: Early Paleogene. FT was sampled from an outcrop near a representative active fault, Atotsugawa Fault, in Japan. Three other granites (OM, RK and ID) were intact blocks cut from quarries. Only TK originated from a drill core, collected in the pilot investigation for an air exchange shaft construction at the Mizunami Geological Center; the TK from 105 to 105.2 m in the core was used for the compression test to avoid the effects of weathering, faulting, and chemical alteration. The granites were regulated into test pieces cylindrical in shape with diameters 5 cm and heights 10 cm except for FT. To select an intact part of the core without visible cracks, the test piece of FT was smaller, with a diameter of 3.5 cm and height of 7 cm. Bulk rock densities of the five granites are almost identical, around 2.6 g cm^{-3} (Table 1).

First, for characterization prior to compression testing, gamma-ray intensities of the specimens were measured by a Germanium semiconductor detector (GMX-25190-P: EG&G ORTEC) to estimate the original abundance of radioelements in the rocks by selecting two γ-decay nuclides, ^{226}Ra (parent of ^{222}Rn) and ^{212}Pb (a daughter product of ^{220}Rn). Their γ-ray intensities (Bq/g) are expressed as I_{226} and I_{212}. Under equilibrium conditions, I_{226} and I_{212} can be regarded as proportional to the total contents of the ^{238}U and ^{232}Th series nuclides, respectively. Details of the measurement method, and transformation from the raw data to γ-ray intensity are described in Koike *et al.* (2014b). The I_{226} and I_{212} values were averaged for multiple specimens of OM, TK and ID. As shown in Table 1, the five granites can be classified into three groups by the similarity of I_{226} and I_{212} values: OM and ID for the weakest intensities, RK and FT for middle-value intensities, and TK for the strongest intensities, which were three times greater than the weakest group. Clearly, the contents of radioelements differ significantly with the locality.

Next, grain size and content ratio of coloured minerals (typically biotite, amphibole, and pyroxene) were measured using parallel- and crossed-Nicols thin-section images. Parts of these thin-sections are shown in Fig. 1. As described below, Rn emanation fraction varies with grain size and mineral species. Importance of coloured minerals is supported by that zircons and monazites with high radium concentrations are included in biotites (Nicolas *et al.* 2014). Although the mean grain sizes are not largely different among the five granites, recognizable features from Table 1 are summarized as follows: the mean grain size of ID (2.3 mm) is slightly larger than the other granites (2–2.1 mm) and that of OM is the smallest (1.5 mm). OM has the largest content ratio of coloured minerals (11.1 per cent), whereas the coloured minerals comprise an extremely small fraction in RK (1.7 per cent). Microcracks are well developed in the quartz grains of FT (Fig. 1), which may be related to the fact that FT is the oldest granite and subjected to repeated and variable tectonic stresses over time.

3 EXPERIMENTAL PROCEDURES

The experimental system was composed of a material testing machine (MTS810), a self-made cell unit for uniaxial compression of specimens, a portable α-scintillation detector (AB-5: Pylon Electrics) for continuous measurement of the Rn concentration before, during, and after the loading, and, a data logger (Fig. 2). The

Table 1. Specifications of granite specimens. Selected mineralogical and mechanical properties with respect to mineral texture, γ-ray intensity, rock strength and failure, and Rn increase are summarized.

Granite name	Number of specimen	Bulk density (mean, g cm^{-3})	Grain size (mean, mm)	Content rate of coloured minerals (per cent)	γ–ray intensity of ^{226}Ra (mean, Bq g^{-1})	γ–ray intensity of ^{212}Pb (mean, Bq g^{-1})	Uniaxial compressive strength (MPa)	Failure pattern	Time to failure (hr)	Stress level at Rn increase start/compressive strength (per cent)
Oshima (OM)	2	2.60	1.5	11.1	35.3 ± 5.5	23.1 ± 0.6	260	Conjugate shear	13.8	51
Rokko (RK)	1	2.59	2.1	1.7	67.7 ± 5.5	43.0 ± 0.5	189	Longitudinal crack	9.5	57
Toki (TK)	5	2.63	2.0	6.1	119.2 ± 3.1	69.7 ± 0.3	146	Longitudinal crack	7.1	46
Fuatsu (FT)	1	2.61	2.1	4.5	66.9 ± 3.9	45.7 ± 0.4	159	Longitudinal crack	4.0	55
Inada (ID)	6	2.64	2.3	4.9	44.7 ± 5.7	35.6 ± 0.7	203	Conjugate shear	5.0	0

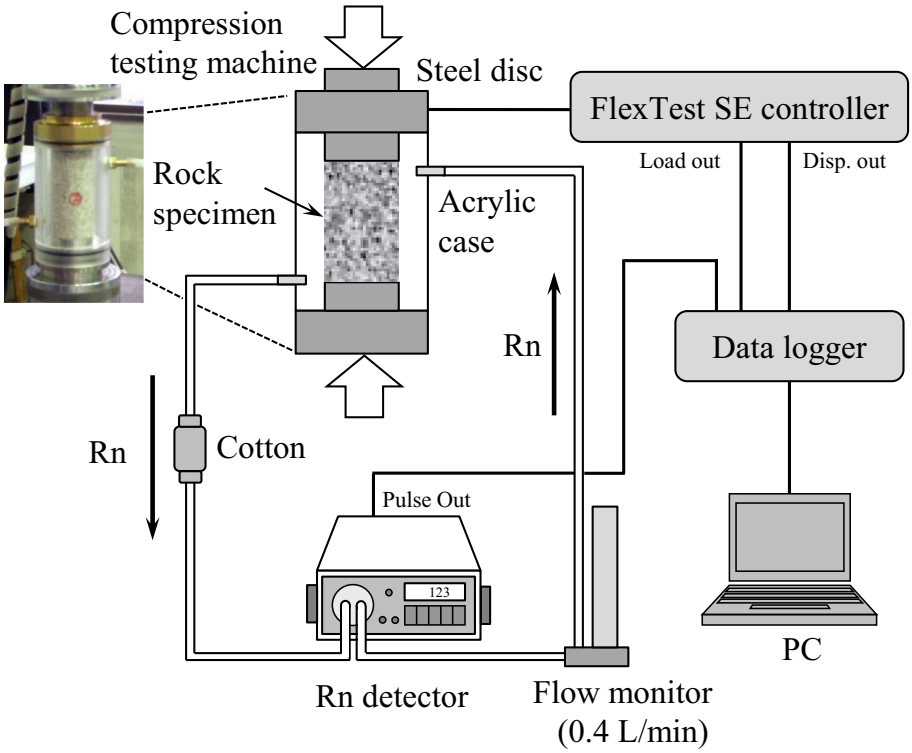

Figure 2. Outline of experimental system. The system is composed of a material testing machine, a cell unit for uniaxial compression of a specimen, a portable α-scintillation detector to continuously measure Rn from specimen, a flow monitor, and a data logger.

testing machine increases the load by controlling increment per unit time at the planned value. The cylindrical cell unit, composed of acrylic board on the side and high carbon steel (JIS S55C) disc cap on the top and bottom ends, was fully confined by filling the gap between the board and disc with the O-ring shaped gum, so as not to leak the gas.

The total number of α particles per minute (cpm) emitted from the specimen, resulting from the decays of ^{222}Rn and ^{220}Rn and their daughter nuclides, ^{218}Po (half-life: 186 s) and ^{216}Po (0.158 s), were counted successively. Gas flow in the cell unit was generated from the inlet and outlet made in the upper and lower parts of the cell, respectively, and the flow was fixed at 0.4 L min^{-1} using the pump installed in the detector. Because Rn is about 7.5 times heavier than air given its density of 9.73 g L^{-1} at 0 °C and 101.325 kPa, the location of the outlet was designed so that Rn could flow out efficiently from the cell. Most α particles probably originated from the decay of ^{222}Rn because of its longest half-life, but this detector did not differentiate the separate contribution of each nuclide. Then, the α particles cpm was simply termed Rn count by assuming that this count was proportional to the true Rn concentration.

Each experiment started with measurement of the background Rn count under constant flow circulation and unloading conditions. After the background counts became stable, compression of the specimen was started and the Rn counts were measured successively with the displacement and stress of the specimen. Recording of the Rn counts was continued after failure of the specimen. All tests were conducted at room temperature.

4 RESULTS

To characterize temporal change in the Rn counts in detail, and to avoid sudden failure of the specimen soon after the start of loading, the tests were implemented under loading control conditions such that the load on specimen was set to increase gradually and linearly at 0.5 kN min^{-1}. The Rn counts were summed successively during 5 min to enhance S/N ratio. Nevertheless the series of total count per 5 min fluctuated largely. The counts were then smoothed by a polynomial to delineate a trend in the count changes. The raw count data and the trend curve are superimposed on the stress change in Fig. 3. Time to failure from the start of loading, and the uniaxial compressive strength (UCS), were widely different among the five granites, from 4 to 13.8 hr and 146 to 260 MPa, respectively (Table 1). OM took the maximums of both the attributes. Failure patterns were roughly grouped into conjugate shear failure type (samples of OM and ID), and tensile failure type with developing longitudinal cracks (samples of RK, TK and FT; Fig. 3).

Note from the trend curves that the Rn counts of four granites (OM, RK, TK and FT) decrease slightly from the background level after the start of loading and then, increase at 46–57 per cent stress level to UCS, except for granite ID. To check the decrease in more detail, only the count data under loading were selected and approximated by polynomials of the same order as all the count data in Fig. 3 (9th order). Fig. 4 highlights that the polynomial regression curves have a better fit to the original Rn counts than to the counts for all the data. Using the regression curves, the decreases in the Rn counts after the start of loading were roughly estimated from the difference between the maximum and minimum of the polynomial curve of the Rn counts before the increase (the two short bars in Fig. 4). The estimations were 15 per cent (OM), 12 per cent (RK), 8 per cent (TK) and 30 per cent (FT). Because cracks in a specimen can be paths of Rn emanation from the grain surfaces and of Rn migration, closure of microcracks is the most rational cause for the initial decrease, as noted by previous researchers cited above. This decrease is analogous to the decline in groundwater-dissolved Rn in near-field sites before the $M = 7$ Izu-Oshima earthquake in Japan (Wakita *et al.* 1980) and the three earthquakes in Taiwan (Kuo

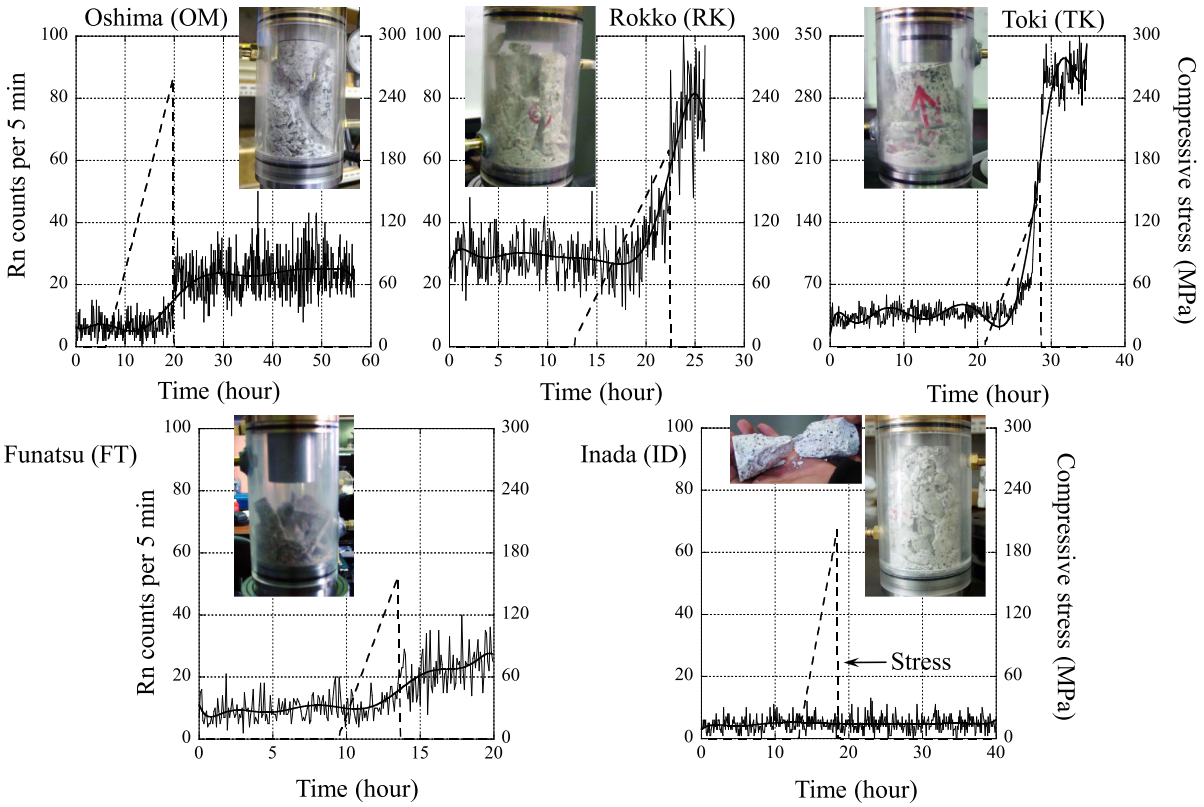

Figure 3. Rn counts with progress of uniaxial compression and their trend curve by polynomial approximation, overlaid on change in compressive stress (broken line). Rn counts correspond to the total number of α particles per 5 min resulting from the decays of ^{222}Rn and ^{220}Rn and their α-decay daughter nuclides, but most are probably originated from ^{222}Rn because of its longest half-life.

et al. 2009, 2013), for which the decline began around 2 months prior to the earthquakes. A similar case is a pre-seismic sharp drop of Rn in the borehole air which was observed few days before an earthquake $M = 4.9$ in India at a borehole located 60 km from the epicentre (Choubey *et al.* 2009). A sharp drop was also observed in groundwater-dissolved Rn in a near-field site 7 d before the $M = 7.2$ Kobe earthquake in Japan (Igarashi *et al.* 1995).

The stress level at the commencement of Rn count increase (around 50 per cent of UCS) corresponds with an increase in microcracking within a specimen (Holub & Brady 1981; Li *et al.* 2003). Through a uniaxial compression test and scanning electron microscopic (SEM) observation, Li *et al.* (2003) found that significant stress-induced cracks start to appear in quartz grains when the applied load attains around 50 per cent of peak stress. These cracks extend rapidly in quartz grains with increasing stress, and align nearly along the loading direction. Therefore, the increase of Rn counts can be ascribed to the enhancements of the numbers and connectedness of micro- and macrocracks (Nicolas *et al.* 2014). The enhancements also extend the rock surface area with increasing stress, which can release Rn atoms enclosed in minerals and extrude them as interpreted by Holub & Brady (1981).

The most remarkable feature in the curves of Fig. 3 is that the Rn counts continue to increase even after failure, except for granite ID. The counts reached maximums at 7 hr after the failure in the cases of OM and FT. This increase phenomenon after failure confirms the findings of preceding studies cited above. Fragmentation of the specimen by failure results in greatly increased rock surface area, which can promote further Rn emanation and migration, and consequently the Rn count is increased. Similar to the present result, enhancements of Rn concentration in soil gas and groundwater in aftershocks have been observed in the near-field and far-field sites of the 2008 $M = 8.0$ Wenchuan earthquake (Ren *et al.* 2012), a far-field site of the 2011 $M = 9.0$ Tohoku earthquake (Tsunomori & Tanaka 2014), and in the abovementioned earthquakes in Taiwan and India (Choubey *et al.* 2009; Kuo *et al.* 2009, 2013).

5 DISCUSSION

To correct for the difference in volume between FT and the other samples, the converged count after failure minus the averaged background count in Fig. 3 was divided by the volume of specimen and termed the gross count increase (GCI). GCI is compared with I_{226} to clarify the correlation between the ^{226}Ra content and the maximum quantity of Rn emission by failure (Fig. 5a). Because GCI and I_{226} of granite TK are extremely larger than the others, a strong correlation seems to hold between them (linear correlation coefficient $R = 0.97$). Despite this bias and the limited number of data, the present result supports a general interpretation that rocks with high radioelement contents induce large Rn emission by fracturing and failure (e.g. Katoh *et al.* 1984, 1985).

Considering an imperceptible recoil distance of Rn, around just 0.1 μm in rocks in the bulk density range of this study (Tanner 1980), the distribution style of radioelements in minerals, such as concentrated near the grain boundaries or scattered in the grains, is a possible factor affecting the Rn emanation quantity to the cracks and fractures. Furthermore, the facts that granites TK, FT and RK were of the tensile failure type and had large GCI are noteworthy (Fig. 5a). Apparently, tensile failure can generate significant space accompanying the many longitudinal cracks, and release stress for the migration of Rn. The failure pattern (whether conjugate shear

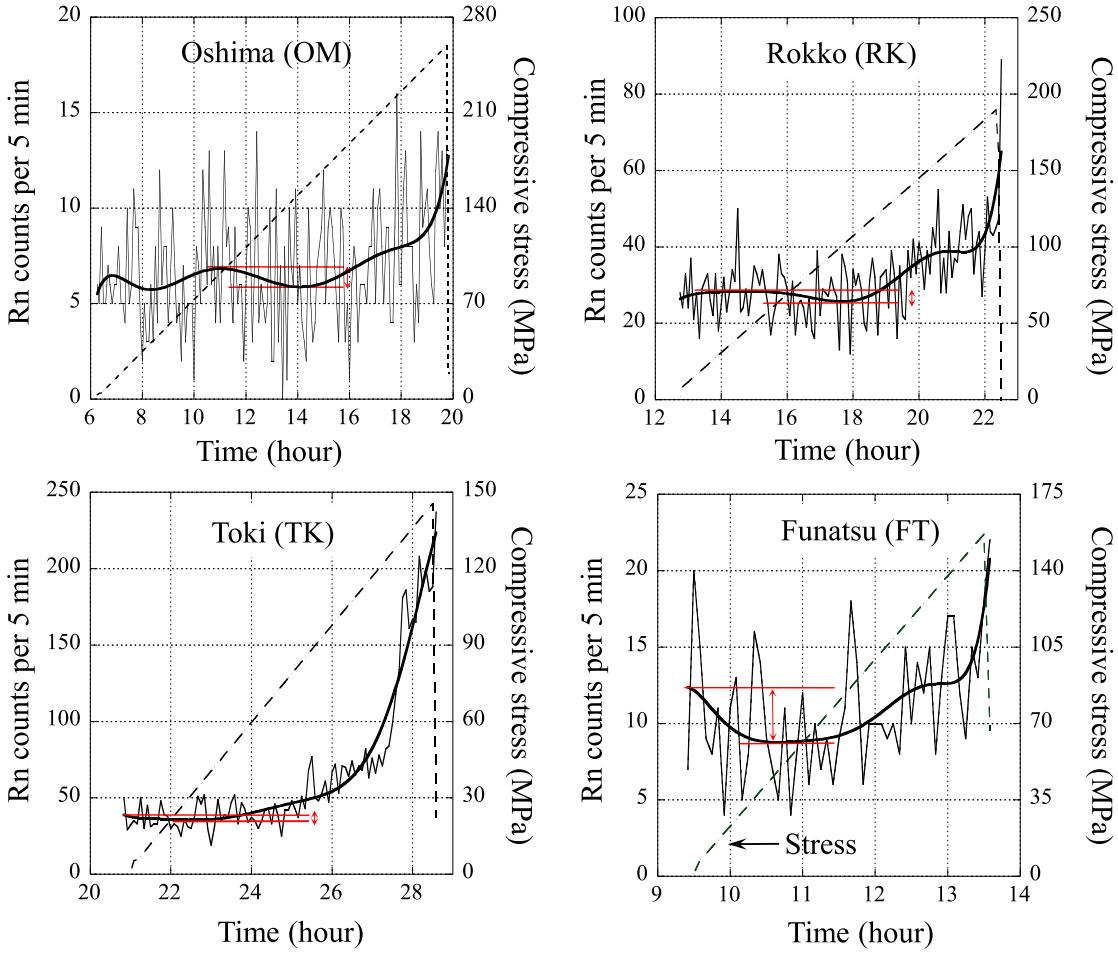

Figure 4. Selected Rn counts under loading only from Fig. 3 and their polynomial regression of the same order as all the counts data (9th order). Four granites that showed increases in the Rn counts with compression and failure were used. The two short bars in each graph indicate the maximum and minimum of the polynomial curve of Rn counts before the increase.

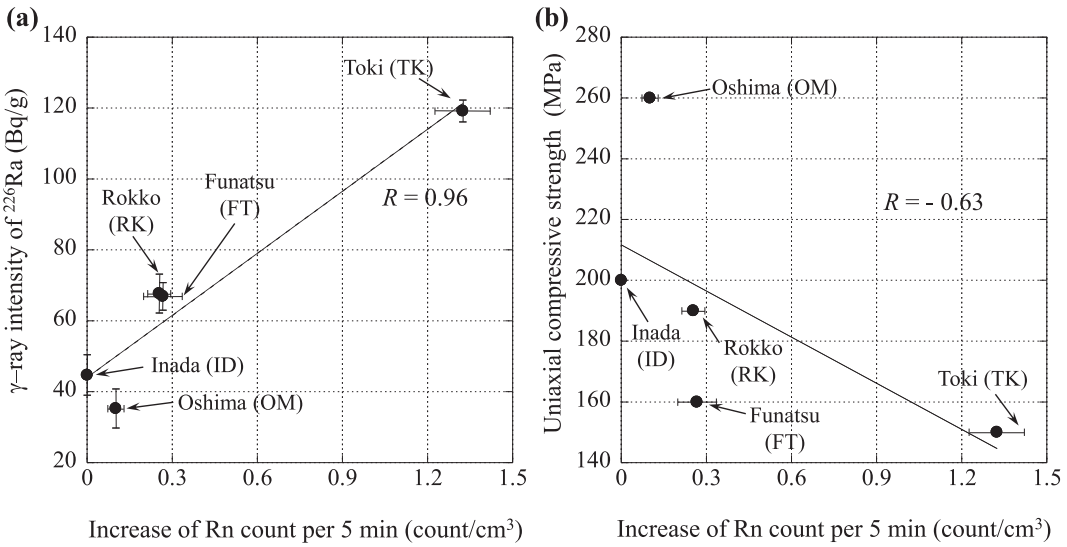

Figure 5. Correlations of gross Rn count increase (GCI) by rock failure with Ra content and rock strength. (a) Horizontal and vertical axes stand for GCI, which is the convergence of Rn counts per 5 min after the failure minus the averaged background counts, and γ-ray intensity of ^{226}Ra per unit specimen weight, respectively. GCI is a value divided by the volume of specimen. (b) Relationship between GCI and uniaxial compressive strength.

or tensile) may relate to the UCS, given that the UCS values of the three tensile-failure granites are smaller than those of the two conjugate shear-failure granites, ID and OM (Table 1). Although the correlation is weak ($R = -0.63$), GCI roughly shows an increase with decreasing UCS (Fig. 5b). Therefore, granite with lower UCS presumably tends to provide a condition for greater Rn emissions associated with the failure. The effect of difference in failure pattern, and the more reliable index of UCS on the Rn emission quantity, are new findings. In the case of soil gas near the ground surface, correlation between Rn concentration and I_{226} is generally weak, and ascent gas velocity for Rn transport becomes the dominant factor of the soil Rn concentration, as demonstrated by Koike *et al.* (2014b).

Although the I_{226} values of OM and ID are close to each other, the large difference in Rn emission by compression must be explained. The absence of Rn emissions from the ID granite is the same result as uniaxial compression testing by Katoh *et al.* (1984). Two mineralogical properties, grain size and mineral composition, are indicated as the plausible cause of absence of Rn emission in the ID granite, as Rn emanation fraction (F), a ratio of Rn atoms that diffuse from the inside of minerals to pore space, is related to these properties. The moisture content in porous media has been demonstrated to have a large effect on F (Nazaroff 1992). To eliminate this effect, all pores are regarded to be dry in the following discussion.

Assuming simply that rock is composed of spherical grains with the same diameter (d μm), the total crack surface area is proportional to squared d: smaller d makes a larger surface area. Under this assumption, and another assumption that Ra exists only on the grain surface, F in this single-gain model is given as (Morawska & Phillips 1993):

$$F = \frac{1}{2}\left(1 + \frac{\lambda}{d}\right), \tag{1}$$

where λ (μm) is recoil length of Rn in the grain. F decreases with increasing d but reaches a constant value of 0.5 for large d (Sakoda *et al.* 2011). Accordingly, F is a function of only grain size for the fixed λ: larger grain size has smaller F and reduces Rn emission. The grain size of granite ID is slightly larger than the others in this study on average (Table 1), and is therefore predicted by eq. (1) to have lower Rn emission. However, the relationship between GCI and the mean grain size becomes meaningless for all the specimens (R is almost zero). The effect of grain size should be studied further by testing granite specimens with different mineral textures.

F is also variable with mineral species. F values of the chief granite-forming minerals were measured by Sakoda *et al.* (2011) with results of: quartz, 0.046; plagioclase, 0.0185; hornblende, 0.0342 and biotite, 0.028–0.066. These values suggest that coloured minerals have larger F values, however, the F values of these minerals cannot be precisely compared with each other because their grain sizes are not the same. In fact, the content rates of coloured minerals of the five granites of this study (Table 1) are not correlated with GCI (R is almost zero). For example, GCI of OM is the second smallest despite the highest content of coloured minerals. The effect of mineral composition on the quantity of Rn emission is uncertain with the present data, but further examination could be useful.

The change of Rn counts with time in the interval between the commencement of count increase and failure can be approximated by a line (Fig. 3). Considering this trend, the gradient of the line (count in 5 min hr^{-1}), termed count increase ratio (CIR), is correlated with GCI (Fig. 6). CIR was normalized to the volume of specimens in the same manner as GCI. Because F is enhanced by

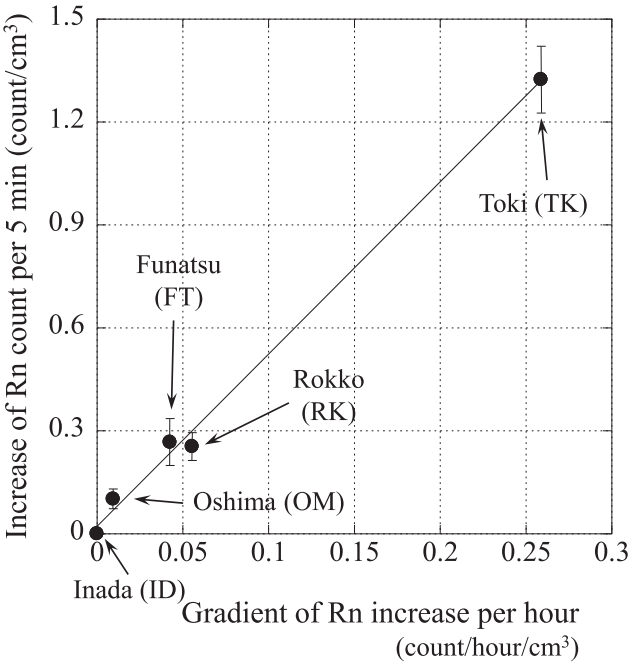

Figure 6. Relationship between GCI and the count increase ratio per unit time and unit volume (CIR). CIR is regarded to have a relationship with development velocity of total crack surface area, that is, Rn emanation area.

increasing the total crack surface area (as shown above), CIR is regarded to be related to development velocity of this area, that is, the Rn emanation area. Three granites of this study, TK, RK and FT, which have relatively large GCI, are confirmed to also have large CIR. Therefore, an additional control factor for the quantity of Rn emission with failure may be a failure progress property of rock: one possibility is development velocity of the total crack surface area, as the present CIR indicates. Higher development velocity of the emanation area can induce larger Rn emission during unit time. Well-developed rock fracturing in a short time would then induce blow-off of Rn atoms, and consequently enhance the total Rn emissions. According to this mechanism, Rn emission per unit rock volume associated with a creep fault movement is most likely low.

Concluding our interpretations based on the results of the current experiments and those of Koike *et al.* (2014b) on active fault areas accompanying microseismicity, Table 2 summarizes the mineralogical and mechanical conditions of crystalline rocks for controlling the change in Rn concentration in soil gas or groundwater at early pre-earthquake stage, and the quantity of Rn increase at pre-failure and post-earthquake stages. The enhancement of ascent gas velocity for Rn transport is required for the large increase of Rn in soil gas in the latter two stages. Because the Rn diffusion coefficient decreases with increasing soil water saturation fraction (Nazaroff 1992), the condition that the soil is not saturated with water up to the near surface is also necessary. Although changes in Rn gas concentrations over 200 per cent have been observed at several distant locations (exceeding 300 km) from earthquakes (Cicerone *et al.* 2009), an absence of coseismic Rn change has also been reported for some earthquakes and locations (e.g. Wakita 1996). Table 2 can be used for understanding the cause of these and other remarkable or unclear responses of Rn emission in conjunction with earthquakes, at observation sites in crystalline rocks such as granite.

Table 2. Conditions on difference in Rn change before and after earthquake. Mineralogical and mechanical conditions for controlling the change in Rn concentration in soil gas or groundwater at early pre-earthquake stage and the quantity of Rn increase at pre-failure and post-earthquake stages are presumed to interpret the difference in Rn responses depending on earthquakes and observation sites.

Early pre-earthquake response		
Rn change	Stress condition	Crack condition
Decline	Strongly compressed area	Closure
Increase	Dilatancy area by tensile stress	Opening

Pre-failure and Post-earthquake responses					
Rn change	Radionuclide content	Grain size	Failure progress velocity	Break pattern	Ascent gas velocity in shallow crust
Large increase	Large	Small	High	Heavy fracturing for large emanation area	High
Small or no increase	Small	Large	Low	Minor and/or regular fracturing for enhancing emanation area	Low

6 CONCLUSIONS

Through a set of uniaxial compression tests of granite specimens and continuous measurement of Rn emissions from the specimens, the main results of this study are summarized as follows.

(1) As found in previous studies, Rn emissions began to increase at 46–57 per cent stress level to the uniaxial compressive strength and continued to increase even after the failure of specimens. The commencement implies the development of microcracks and concurrent formation of Rn transport paths to the rock surface. Failure enhances the total rock surface area and the Rn emanation from grains and migration, which is accordant with a phenomenon of Rn concentration enhancement in aftershocks, globally observed.

(2) Generally, radioelement content in granite is a main factor for the total increase in Rn emission by failure. Grain size and uniaxial compressive strength associated with failure pattern (conjugate shear or longitudinal tensile type) are likely other control factors. Tensile failure type with lower compressive strength generates abundant space and stress release, and smaller grain size enhances the Rn emanation fraction, which together contribute to increased Rn emission and migration.

(3) Development velocity of the emanation area accompanying the rock fragmentation also has potential to control the total increase in Rn emission by failure, because the Rn emanation may be proportional to the area.

(4) In addition to the magnitude of an earthquake and its hypocentre distance to Rn detectors, the magnitude of increase in Rn concentration in soil gas and groundwater before, during, and after an earthquake in crystalline rocks depends on the intrinsic radioelement content, the mineral texture, and the mechanical properties of rocks.

ACKNOWLEDGEMENTS

Authors are sincerely grateful to Mr Norio Sakamoto and Mr Takayoshi Ueyama, who gave devoted assistance in this study, Prof Yuzo Obara and Assoc Prof Akira Sato of Graduate School of Science and Technology, Kumamoto University for permission to use the test machine and valuable guidance, and Mr Jitsuya Uemura of the Radioisotope Center of Kumamoto University for instruction in measuring γ-ray spectra. Sincere thanks are extended to the two anonymous reviewers for their valuable comments and suggestions that helped us to improve the clarity of the manuscript.

REFERENCES

Asaue, H., Koike, K., Yoshinaga, T. & Takakura, S., 2007. Characterizing deep resistivity structures of Futagawa-Hinagu faults belt and discussion on their relationship with micro-earthquakes distribution, *J. Japan Soc. Eng. Geol.,* **48,** 180–191. (in Japanese with English abst.)

Choubey, V.M., Kumar, N. & Arora, B.R., 2009. Precursory signatures in the radon and geohydrological borehole data for M4.9 Kharsali earthquake of Garhwal Himalaya, *Sci. Total Environ.,* **407,** 5877–5883.

Cicerone, R.D., Ebel, J.E. & Britton, J., 2009. A systematic compilation of earthquake precursors, *Tectonophysics,* **476,** 371–396.

Cigolini, C., Laiolo, M. & Coppola, D., 2007. Earthquake–volcano interactions detected from radon degassing at Stromboli (Italy), *Earth Planet. Sci. Lett.,* **257,** 511–525.

Connor, C., Hill, B., LaFemina, P., Navarro, M. & Conway, M., 1996. Soil ^{222}Rn pulse during the initial phase of the June-August 1995 eruption of Cerro Negro, Nicaragua, *J. Volc. Geotherm. Res.,* **73,** 119–127.

Hishinuma, T., Nishikawa, T., Shimoyama, T., Miyajima, M., Tamagawa, Y. & Okabe, S., 1999. Emission of radon and thoron due to the fracture of rock, *Il Nuovo Cimento,* **22C,** 523–527.

Holub, R.F. & Brady, B.T., 1981. The effect of stress of radon emanation from rock, *J. Geophys. Res.,* **86,** 1776–1784.

Igarashi, G., Saeki, S., Takahata, N., Sumikawa, K., Tasaka, S., Sasaki, Y., Takahashi, M. & Sano, Y., 1995. Ground-water radon anomaly before the Kobe earthquake in Japan, *Science,* **269,** 60–61.

Iidaka, T., Kato, A., Kurashimo, E., Iwasaki, T., Hirata, N., Katao, H., Hirose, I. & Miyamachi, H., 2009. Fine structure of *P*-wave velocity distribution along the Atotsugawa fault, central Japan, *Tectonophysics,* **472,** 95–104.

İnan, S., Akgül, E., Seyis, C., Saatçılar, R., Baykut, S., Ergintav, S. & Baş, M., 2008. Geochemical monitoring in the Marmara region (NW Turkey): a search for precursors of seismic activity, *J. Geophys. Res.,* **113,** B03401, doi:10.1029/2007JB005206.

Jordan, T.H. *et al.*, 2011. Operational earthquake forecasting: state of knowledge and guidelines for utilization, *Ann. Geophys.-Italy,* **54,** 319–391.

Katoh, K., Ikeda, K., Kusunose, K. & Nishizawa, O., 1984. An experimental study of radon (^{222}Rn and ^{220}Rn) emanated from granite specimens under uniaxial compression, *Bull. Geo. Surv. Japan,* **35,** 1–11. (in Japanese with English abst.)

Katoh, K., Nishizawa, O., Kusunose, K. & Ikeda, K., 1985. An experimental study on variation of radon emanation from Westerly granite under

uniaxial compression Part 1, *Zisin (J Seismological Society of Japan. 2nd ser.),* **38,** 173–182. (in Japanese with English abst.)

King, C.-Y. & Luo, G., 1990. Variations of electric resistance and H_2 and Rn emissions of concrete blocks under increasing uniaxial compression, *Pure appl. Geophys.,* **134,** 45–56.

Koike, K., Yoshinaga, T. & Asaue, H., 2009. Radon concentrations in soil gas, considering radioactive equilibrium conditions with application to estimating fault-zone geometry, *Environ. Geol.,* **56,** 1533–1549.

Koike, K., Yoshinaga, T. & Asaue, H., 2014a. Characterizing long-term radon concentration changes in a geothermal area for correlation with volcanic earthquakes and reservoir temperatures: a case study from Mt. Aso, southwestern Japan, *J. Volc. Geotherm. Res.,* **275,** 85–102.

Koike, K., Yoshinaga, T., Ueyama, T. & Asaue, H., 2014b. Increased radon-222 in soil gas because of cumulative seismicity at active faults, *Earth Planet Space,* **66**(57), 1–9.

Kuo, T. *et al.*, 2009. Radon anomalies precursory to the 2003 $M_w = 6.8$ Chengkung and 2006 $M_w = 6.1$ Taitung earthquakes in Taiwan, *Radiat. Meas.,* **44,** 295–299.

Kuo, T. *et al.*, 2013. Concurrent concentration declines in groundwater-dissolved radon, methane and ethane precursory to 2011 M_w 5.0 Chimei earthquake, *Radiat. Meas.,* **58,** 121–127.

Li, L., Lee, P.K.K., Tsui, Y., Tham, L.G. & Tang, C.A., 2003. Failure process of granite, *Int. J. Geomech.,* **3,** 84–98.

Mollo, S., Tuccimei, P., Heap, M.J., Vinciguerra, S., Soligo, M., Castelluccio, M., Scarlato, P. & Dingwell, D.B., 2011. Increase in radon emission due to rock failure: an experimental study, *Geophys. Res. Lett.,* **38,** L14304, doi:10.1029/2011GL047962.

Morawska, L. & Phillips, C.R., 1993. Dependence of the radon emanation coefficient on radium distribution and internal structure of the material, *Geochim. Cosmochim. Acta.,* **57,** 1783–1797.

Nazaroff, W.W., 1992. Radon transport from soil to air, *Rev. Geophys.,* **30,** 137–160.

Neri, M., Behncke, B., Burton, M., Galli, G., Giammanco, S., Pecora, E., Privitera, E. & Reitano, D., 2006. Continuous soil radon monitoring during the July 2006 Etna eruption, *Geophys. Res. Lett.,* **33,** L24316, doi:10.1029/2006GL028394.

Neri, M., Giammanco, S., Ferrera, E., Patanè, G. & Zanon, V., 2011. Spatial distribution of soil radon as a tool to recognize active faulting on an active volcano: the example of Mt. Etna (Italy), *J. Environ. Radioact.,* **102,** 863–870.

Nicolas, A., Girault, F., Schubnel, A., Pili, É., Passelègue, F., Fortin, J. & Deldicque, D., 2014. Radon emanation from brittle fracturing in granites under upper crustal conditions, *Geophys. Res. Lett.,* **41,** 5436–5443.

Ren, H.W., Liu, Y.W. & Yang, D.Y., 2012. A preliminary study of post-seismic effects of radon following the Ms 8.0 Wenchuan earthquake, *Radiat. Meas.*, **47,** 82–88.

Sakoda, A., Ishimori, Y. & Yamaoka, K., 2011. A comprehensive review of radon emanation measurements for mineral, rock, soil, mill tailing and fly ash, *Appl. Radiat. Isotopes,* **69,** 1422–1435.

Scholz, C.H., Sykes, L.R. & Aggarwal, Y.P., 1973. Earthquake prediction: a physical basis, *Science,* **181,** 803–810.

Tanner, A.B., 1980. Radon migration in the ground: a supplementary review, in *Proceedings of the Natural Radiation Environment III,* April 23–28, 1978, Houston, TX, pp. 5–56.

Tsunomori, F. & Tanaka, H., 2014. Anomalous change of groundwater radon concentration monitored at Nakaizu well in 2011, *Radiat. Meas.,* **60,** 35–41.

Tuccimei, P., Mollo, S., Vinciguerra, S., Castelluccio, M. & Soligo, M., 2010. Radon and thoron emission from lithophysae-rich tuff under increasing deformation: an experimental study, *Geophys. Res. Lett.,* **37,** L05305, doi:10.1029/2009GL042134.

Wakita, H., 1996. Geochemical challenge to earthquake prediction, *Proc. Natl. Acad. Sci. U.S.A.,* **93,** 3781–3786.

Wakita, H., Nakamura, Y., Notsu, K., Noguchi, M. & Asada, T., 1980. Radon anomaly: a possible precursor of the 1978 Izu-Oshima-kinkai earthquake, *Science,* **207,** 882–883.

Wang, X., Li, Y., Du, J. & Zhou, X., 2014. Correlations between radon in soil gas and the activity of seismogenic faults in the Tangshan area, North China, *Radiat. Meas.,* **60,** 8–14.